



저작자표시-비영리-변경금지 2.0 대한민국

이용자는 아래의 조건을 따르는 경우에 한하여 자유롭게

- 이 저작물을 복제, 배포, 전송, 전시, 공연 및 방송할 수 있습니다.

다음과 같은 조건을 따라야 합니다:



저작자표시. 귀하는 원저작자를 표시하여야 합니다.



비영리. 귀하는 이 저작물을 영리 목적으로 이용할 수 없습니다.



변경금지. 귀하는 이 저작물을 개작, 변형 또는 가공할 수 없습니다.

- 귀하는, 이 저작물의 재이용이나 배포의 경우, 이 저작물에 적용된 이용허락조건을 명확하게 나타내어야 합니다.
- 저작권자로부터 별도의 허가를 받으면 이러한 조건들은 적용되지 않습니다.

저작권법에 따른 이용자의 권리는 위의 내용에 의하여 영향을 받지 않습니다.

이것은 [이용허락규약\(Legal Code\)](#)을 이해하기 쉽게 요약한 것입니다.

[Disclaimer](#)

이학석사 학위논문

Hemispherically asymmetric
response of Hadley-cell edge to
the CO₂ removal scenario

이산화탄소 증가 및 감소에 따른
해들리셀 경계의 비대칭적인 반응

2022년 8월

서울대학교 대학원

협동과정 계산과학

최 영 주

Hemispherically asymmetric
response of Hadley-cell edge to
the CO₂ removal scenario

이산화탄소 증가 및 감소에 따른
해들리셀 경계의 비대칭적인 반응

지도 교수 손 석 우

이 논문을 이학석사 학위논문으로 제출함
2022년 7월

서울대학교 대학원
협동과정 계산과학
최 영 주

최영주의 이학석사 학위논문을 인준함
2022년 8월

위 원 장 _____ 허 창 회 (인)

부위원장 _____ 손 석 우 (인)

위 원 _____ 박 록 진 (인)

Abstract

The poleward shift of the Hadley cell (HC) edge by global warming is widely documented. However, most previous studies have focused on the HC changes in response to the increasing CO₂ forcing. We investigate the HC changes in response to the transient reversibility of the CO₂ forcing by conducting a climate model experiment where CO₂ concentration is systematically increased and then decreased in time. It is found that a poleward-shifted HC edge in a warm climate returns equatorward as CO₂ concentration decreases, and the rate significantly differs between the two hemispheres. While the southern HC edge monotonically changes with CO₂ concentration, the northern HC edge exhibits a super recovery, located on the equatorward side of the present-climate HC edge when CO₂ concentration returns to the present level. Such a super recovery is associated with the hysteresis of the North Atlantic sea surface temperature. Our findings suggest that the HC edge change may result in the super recovery of subtropical dryness in the northern hemisphere.

Keywords: Hadley cell, transient CO₂ experiment, baroclinicity

Student Number: 2020–24660

Table of Contents

1. Introduction.....	1
2. Data and Methods	4
2.1. Data	4
2.2. Hadley-cell edge	5
2.3. Linear baroclinicity	6
2.4. Global Dryness Index.....	8
3. Results	9
3.1 Climate components changes	9
3.2 Hadley-cell changes	10
3.3 Possible mechanisms for the HC-edge responses.....	13
3.4 Hydro-climate implication of the HC change	16
4. Summary and Discussions.....	18
References.....	21
Figures.....	27
Abstract in Korean	37

List of Figures

Fig. 1. Time series of CO₂ concentration (black), global mean sea surface temperature (SST, red), and global mean precipitation (PRCP, blue), respectively. Red and blue solid lines indicate the 28-member ensemble mean, and a black horizontal line indicates the PD state of CO₂ concentration.

Fig. 2. Spatial distribution for the 28-ensemble mean of the zonal-mean temperature (units: °C) changes. (a) is the changes during the RU period computed by PEAK (2120–2160) minus earlyRU (2001–2040), and (b) is during the RD period computed by the lateRD (2241–2280) minus PEAK (2120–2160). (c) is the difference between RST period (2281–2320) and PD state. Contours indicate the climatology in the PD experiment and hatching denotes regions where the difference is statistically insignificant based on Student's *t*-test estimates at the 95% level.

Fig. 3. Spatial distribution for the 28-ensemble mean of meridional streamfunction (units: 10¹⁰ kg s⁻¹) changes. (a) is the changes during the RU period computed by PEAK (2120–2160) minus earlyRU (2001–2040), and (b) is during the RD period computed by the lateRD (2241–2280) minus PEAK (2120–2160). (c) is the difference between RST period (2281–2320) and PD state. Contours indicate the climatology in the PD experiment and hatching denotes

regions where the difference is statistically insignificant based on Student' s t-test estimates at the 95% level.

Fig. 4. The HC edge changes in (a), (c) the southern hemisphere, and (b), (d) the northern hemisphere. (a), (b) the time evolutions of the HC edge for a changing CO₂ pathway. The thick solid lines and shadings denote the mean and one-standard deviation range of 28 ensembles smoothed with an 11-yr running mean, respectively. The mean and one-standard deviation range in the PD run are denoted by horizontal solid and dashed lines, respectively. (c), (d) the relationship between changes of the HC edge during the RU and RD period. Changes during the RU and RD period are computed by PEAK (2120–2160) minus earlyRU (2001–2040), and by lateRD (2241–2280) minus PEAK. Blue and green symbols indicate the results of CESM-LE and CMIP6, respectively.

Fig. 5. Time evolution of baroclinicity anomalies over the (a) southern and (b) northern hemispheres relative to the PD run. The solid and dashed lines denote the mean of 28 ensembles, and shadings indicate the one-standard deviation range of that. Purple, red, and blue correspond to the baroclinicity changes due to both static stability and wind shear, only due to static stability, and only due to wind shear, respectively.

Fig. 6. Spatial distribution for the 28-ensemble mean of sea surface

temperature (SST, units: $^{\circ}$ C) changes. (a) is the changes during the RU period computed by PEAK (2120–2160) minus earlyRU (2001–2040), and (b) is during the RD period computed by lateRD (2241–2280) minus PEAK (2120–2160). (c) is the difference between RST period (2281–2320) and PD state. Contours indicate the climatology in the PD experiment and hatching denotes regions where the difference is statistically insignificant based on Student's t-test estimates at the 95% level.

Fig. 7. (a) Time evolution of SST gradient anomalies (units: $^{\circ}$ C) relative to the PD run over the Southern hemisphere (SH; black). (b) Same as (a) but for the Northern hemisphere (NH; black), the North Pacific (NP; 120° E – 90° W, pink dashed), and the North Atlantic (NA; 70° W– 20° E, red dashed). The SST gradient implies the latitudinal gradient calculated by the SST differences from the tropics (0° – 15° latitude) to the mid-latitudes (45° – 60° latitude) in each hemisphere. The solid and dashed lines denote the 28-member ensemble mean smoothed with an 11-yr running mean, and shadings indicate the one-standard deviation range of that.

Fig. 8. Spatial distribution for the 28-ensemble mean of the GDI (left, unit: months year $^{-1}$) and zonal-mean P–E changes (right, units: mm day $^{-1}$). (a), (d) is the changes during RU period computed by PEAK (2120–2160) minus earlyRU (2001–2040), and (b), (e) is during the RD period computed by the lateRD (2241–2280) minus PEAK (2120–2160). (c), (f) is the difference between RST (2280 - 2320) and PD

state. Contours in (a)–(c) are the climatological GDI in the PD experiment. Dotted regions denote the statistically insignificant difference based on Student’ s t-test estimates at the 95% level. The colored area in (d)–(f) indicates negative (brown) and positive (green) P–E differences ($\delta P-E$), and black lines denote the climatological zonal–mean P–E in the PD experiment.

Fig. 9. Time evolution of the GDI peak in (a) southern and (b) northern hemispheres, and (c) ITCZ for a changing CO₂ pathway. The thick solid lines and shadings denote the mean and one–standard deviation range of 28 ensembles smoothed with an 11–yr running mean, respectively. The mean and one–standard deviation range in the PD run are denoted by horizontal solid and dashed lines, respectively.

1. Introduction

Global climate is largely associated with a zonal–mean meridional atmospheric circulation known as the Hadley cell (HC), which consists of the ascending branch of moist air in the deep tropics, the poleward flow aloft, the descending branch of dry air in the subtropics, and the equatorward flow near the surface. The ascending branch in equatorial regions promotes tropical rainfall, and the descending branch at the poleward edge of the HC determines the subtropical dry zone. As the HC has a considerable impact on the global and regional hydro–climate system (Seidel et al. 2007; Feng and Fu 2013), changes in the HC have been studied in the sense of observation and climate models.

Observation evidence typically indicates that the HC width has expanded poleward since 1979, despite varying the expanding rate from 0.2° – 0.6° latitude decade⁻¹ (Allen et al. 2014; Davis and Birner 2017; Grise et al. 2018; Staten et al. 2018), which based on satellite and radiosonde, and reanalysis. In climate models, the HC expansion is also found in a larger extent compared to the observed trends (Adam et al. 2014; Grise et al. 2018).

The mechanisms of HC change in response to global warming are complicated due to the roles of anthropogenic forcings (e.g., Hawkins and Sutton 2009; Staten et al. 2018). A series of studies

documented that the increasing greenhouse gases (GHGs), e.g., CO₂, is a primary cause of the observed and projected global warming trends during the recent half-century. The increasing CO₂ greatly affects the HC expansion, especially in the SH (Watt-Meyer 2019), through an increase in the subtropical static stability (e.g., Lu et al. 2008; Son et al. 2018b). However, the HC response has been rarely investigated under possible CO₂ removal over the coming decades. Although a few studies explored the atmospheric response to the decrease of CO₂ in the equilibrium state (D'Agostino 2018; Son et al. 2018b; Kim and Son 2020), the HC response to transiently removed CO₂ after its increase is not studied. One of the questions of interest about CO₂ removal is the reversibility of the atmospheric circulation changes. If it is not reversible, what drives such irreversibility and when it would be recovered are remained open questions.

Here we attempt to address how the HC edge would respond to future CO₂ removal using large ensembles of Community Earth System Model 1.2.2 (CESM1) experiments. Unlike the previous research which has focused on the response of the HC to the increasing CO₂ (e.g., Hu et al 2013, Son et al. 2018a), By performing the idealized transient CO₂ increase and removal (CDR) experiments and using 28 ensemble simulations of the CESM1, the recovery of the Hadley-cell edges in both hemispheres in response to CO₂

removal is investigated.

2. Data and Methods

2.1. Data

In this study, we use the Community Earth System Model version 1.2 (CESM1.2; Hurrell et al. 2013), which consists of the atmosphere (Community Atmospheric Model version 5, CAM5), ocean (Parallel Ocean Program version 2, POP2), sea ice (Community Ice Code version 4, CICE4), and land models (Community Land Model version 4, CLM4). The horizontal resolution of the atmospheric model is $1^\circ \times 1^\circ$ and 30 vertical levels, and that of the ocean model is $1^\circ \times 0.5^\circ$ with 60 vertical levels. The land model uses the carbon–nitrogen cycle.

For the CESM1.2, the equilibrium and transient CO_2 simulations are performed. As an equilibrium simulation, a present–day (PD) experiment is performed over 900 years with a constant CO_2 concentration of 367 ppmv, the present–day CO_2 concentration. We split the PD experiment into 20 years on each of the 28–member ensembles. A transient CO_2 simulation is conducted with each 28–member ensemble in a changing CO_2 pathway, as shown in Fig. 1a with a black solid line.

in which the CO_2 concentration increased 1% per year until it is quadruple its initial level (ramp–up period; RU) and immediately decreased by the same rate symmetrically until it reaches the initial

level (ramp-down period; RD). Subsequently, an equilibrium simulation with the initial CO₂ concentration (367 ppmv) is conducted in the 28-member ensemble for 220 years, referred to as the restoring period (RST). The 28 ensemble members are identical except for the initial atmospheric and oceanic conditions with different phases of the Pacific Decadal Oscillation and Atlantic Multidecadal Oscillation based on the PD simulation.

To examine the consistency of the large-ensemble analysis of CESM1.2, seven models (ACCESS-ESM1-5, CanESM5, CESM2, GFDL-ESM4, MIROC-ES2L, NorESM2-LM, and UKESM1-0-LL) are used from the Coupled Model Intercomparison Project Phase 6 (CMIP6; Eyring et al. 2016; Keller et al. 2018). The equilibrium and transient CO₂ simulations in the CMIP6 are identical to that in the CESM1.2, except for the initial CO₂ concentration level of 284.7 ppmv as the pre-industrial CO₂ concentration.

2.2. Hadley-cell edge

A mean meridional overturning circulation in the tropics, known as the HC, is generally measured by the mean meridional streamfunction. The HC edges locate the latitude where the mean meridional streamfunction reaches zero in terms of mass conservation. The zero-crossing latitude of the 500 hPa mass streamfunction is generally used to estimate the HC edge, which is

called $\Psi 500$ metric. We used this $\Psi 500$ metric, following Hu and Fu (2007), and Waugh et al. (2018).

$$\Psi 500 = \frac{2\pi a \cos\phi}{g} \int_{0 \text{ hPa}}^{500 \text{ hPa}} \overline{[v]} dp$$

where overbars and square brackets are the time mean and the zonal mean, respectively, and others are follows the standard symbols in the atmosphere.

For comparison, we also define the HC edge using other metrics such as the zero crossing of zonal mean surface zonal wind and the zero crossing of zonal mean precipitation minus evaporation (Waugh et al., 2018). The HC width is defined as the latitudinal range between the southern and northern HC edges.

2.3. Linear baroclinicity

Following the earlier studies (e.g., Held 2000; Walker and Schneider 2006; Lu et al. 2008; Tandon et al. 2013), the change of HC edge can be explained by the baroclinic instability theory that the angular momentum conserving flow in the upper troposphere, which extends poleward until the vertical shears become baroclinically unstable, determines the poleward extent of the HC edge. We utilize the following baroclinic criticality formulation of Phillips (1954) quantifying the baroclinicity (C) of the theory,

$$C \equiv \frac{f^2 \Theta_0}{\beta g H} \frac{U_z}{\theta_z} = \frac{f^2 \Theta_0}{\beta g H} \frac{(U_{z,PD} + U_z^*)}{(\theta_{z,PD} + \theta_z^*)}, \quad (1)$$

where U_z and θ_z are the bulk vertical wind shear ($U_z = U_{500} - U_{850}$) and the bulk static stability ($\theta_z = \theta_{500} - \theta_{850}$) during a changing CO₂ pathway calculated with zonal fields at 500 and 850 hPa, respectively. The subscript of PD means the PD mean state, and * denotes the deviation from the PD mean state. Following Lu et al. (2008), both U_z and θ_z are averaged over the subtropics (20° – 40° latitude) for each hemisphere. The Coriolis parameter f and its latitudinal gradient β and gravity g are constant, and other variables are set to a constant (i.e., thickness of the air column H between 500 and 850 hPa is 5000m, and the reference potential temperature Θ_0 is 300K).

By assuming that the bulk static stability changes in response to a changing CO₂ pathway from the PD states (θ_z^*) are much smaller than the PD states of static stability ($\theta_{z,PD}$), the baroclinicity (C) in Eq. (1) can be approximated as below,

$$C \cong C_{PD} \left(1 + \frac{U_z^*}{U_{z,PD}} - \frac{\theta_z^*}{\theta_{z,PD}} \right), \quad (2)$$

Then the change of baroclinicity from the PD mean state (δC_{all}) can be decomposed into the contribution by bulk static stability changes (δC_{st}) and by bulk vertical wind shear changes (δC_{ws}).

$$\delta C_{all} = \delta C_{ws} + \delta C_{st}, \quad (3)$$

$$\text{where } \delta C_{ws} = C_{PD} \frac{U_z^*}{U_{z,PD}}, \quad \delta C_{st} = -C_{PD} \frac{\theta_z^*}{\theta_{z,PD}}$$

The δ term means the difference of the change in a changing CO₂

pathway from the PD states. It is verified that the approximation applied in Eq. (2) is appropriate by the comparison of the baroclinicity change (δC) with the approximated (δC_{all}).

2.4. Global Dryness Index

To investigate the regional structure of the hydrological change, the GDI is computed by the frequency of the occurrence of dry months defined as a month where the monthly rainfall is less than 0.5 mm day^{-1} (Polade et al., 2014; Lau and Kim, 2015). This is one of the effective quantities to detect the global warming signal in the water cycle, measuring an extremely dry climate. The climatological GDI map matches well with regions of low P-E field.

3. Results

3.1. Climate components changes

In this section, we investigate the behaviors of the climate components such as sea surface temperature (SST), precipitation (PRCP), and zonal-mean atmospheric temperature in response to a changing CO₂ pathway (black). Figure 1. shows the time evolution of global mean SST (red) and PRCP (blue) for the 28-ensemble mean in a changing CO₂ pathway (black). Both SST and PRCP exhibit systematic responses to the increasing and decreasing CO₂ changes. Although the CO₂ concentration starts to decrease, both of them continue to increase for several years, and the PRCP reaches its peak more slowly than SST. It is known that the delayed response to CO₂ forcing results from the thermal inertia of the ocean (Wigley, 2005, Boucher et al., 2012). During the ramp-down (RD) period, the declines are much slower than the rises in SST and PRCP, and they eventually do not return to their original state of the PD experiment.

From the spatial distribution of zonal-mean air temperature changes (Fig. 2), it is found that the change of the zonal-mean air temperature in the changing CO₂ pathway is different in both hemispheres. The troposphere generally warms up and cools down (Fig. 2a and 2b) in both hemispheres during increasing and decreasing CO₂ concentration. A noticeable difference in response to

CO₂ forcing between the hemispheres is found in the high latitude, in which a strongly amplified thermal change appears in the Northern Hemisphere (NH), not in the Southern Hemisphere (SH). It is reasonable to expect the hemispheric asymmetry of changes in the latitudinal temperature gradient to CO₂ forcing. During the ramp-up (RU) period, air temperature over the Arctic largely increases, known as the Arctic amplification. Previous studies suggest that it can explain the positive lapse rate feedback in the Arctic (Pithan and Mauritsen, 2014), positive sea ice–albedo feedback (Manabe and Stouffer, 1980), and increased energy transport into the Arctic (Alexeev et al., 2005). In the SH, the warming in the high latitude is not dominant as in the NH, because the upwelling in the Southern Ocean reduces the high–latitude surface warming (Marshall et al., 2014). Furthermore, upper tropospheric temperature exhibits a substantial response to CO₂ forcing. It is known that the increase of the subtropical static stability, the difference in potential temperature between the surface and the tropopause, is able to shift the HC edge poleward (Frierson et al., 2007; Lu et al., 2007). After CO₂ concentration recovers to its PD state, both the troposphere and southern troposphere temperature remains relatively warmer than their PD states (Fig. 2c).

3.2. Hadley–cell changes

To understand the response of the HC to the CO₂ forcing, we investigate changes in the meridional mass streamfunction during each period. Note that the negative and positive mass streamfunction indicate the counterclockwise circulation in the SH and the clockwise circulation in the NH, respectively, which is known as the HC. While the temperature exhibits the linear response to the CO₂ forcing, the meridional mass streamfunction changes less linearly (Fig. 3). During the RU period, the negative and positive change of mass streamfunction appear at approximately 30S and 30N, respectively (Fig. 3a). This implies that the zero-crossing latitude of the mass streamfunction shift poleward as CO₂ increases. In the tropical upper troposphere, the negative and positive mass streamfunction in each hemisphere is strengthened, indicating the upward expansion of the circulation. It is consistent with previously published results (Lu et al., 2007; Johanson and Fu, 2009). During the RD period, the widened and upward expanded circulation is compressed in both hemispheres (Fig. 3b). Compared to the magnitude of the changes during the RU period in each hemisphere, the recovery in the NH is large while that in the SH is small. Figure 3c. shows that the meridional mass streamfunction in the SH is less recovered despite the CO₂ concentration returning to its initial state.

The response of the HC edge latitude in both hemispheres to the changing CO₂ forcing illustrated in Fig. 4. Similar to the documented

results that the HC expansion exhibits a hemispheric asymmetry in a warming climate (Grise et al., 2019; Watt–Meyer et al., 2019), the HC in the NH responds to the increasing and decreasing CO₂ forcing within a range smaller than that in the SH. The location of HC edges after CO₂ recovery also indicates a notable difference between hemispheres.

The southern HC edge, which is located at $31.5 \pm 0.4^\circ$ S during the PD period, moves poleward by 32.6° S with a trend of 0.08° S decade⁻¹ as CO₂ increases (Fig. 4a). Subsequently, the reduction of CO₂ concentration does not lead to an instantaneous recovery of the southern HC edge, and it starts moving equatorward with a trend of -0.08° S decade⁻¹ after a delay of several decades. Although the CO₂ concentration recovers to its initial state, the HC edge in the southern hemisphere (SH) does not completely return to its PD states and remains on the slightly poleward side of its states. It implies that the change of the southern HC edge in the RD period is less slow than that in the RU period.

In the NH, the HC edge is located at $30.0 \pm 0.4^\circ$ N during the PD period. Its expansion in response to increasing CO₂ is $\sim 0.4^\circ$ N, which is smaller than that in the SH. As CO₂ concentration starts to recover, the northern HC edge shifts equatorward with a faster rate of 0.04° decade⁻¹ against its expanding trend of 0.03° N decade⁻¹, showing the early recovery at the 2200s. Despite a short rebound at

the end of the RD period, the HC edge finally is located on the farther equatorward side of its PD state.

3.3. Possible mechanisms for the HC edge responses

The changes in the HC edge are primarily affected by the baroclinic eddies (e.g., Walker and Schneider 2006). Previous studies argued that a poleward shift of the HC edge stems from the increasing static stability and decreasing vertical wind shear under global warming (e.g., Lu et al. 2008, Son et al. 2018b). We further examine the linear baroclinicity, which is a function of dry static stability and vertical wind shear, in response to decreasing CO₂ as well as increasing CO₂. The relative contributions of static stability and vertical wind shear are investigated by quantifying the baroclinicity changes due to static stability, and due to vertical wind shear.

Figure 5a reveals that the change of the southern HC edge is largely determined by the static stability–induced baroclinicity change. This is particularly shown in the SH. The systematic increase and decrease in static stability, in RU and RD periods, respectively, are related to the systematic shifts of the southern HC edge poleward and equatorward (red in Fig. 5a). This result suggests that the equatorward shift of the HC edge in the RD period is likely caused by reduced subtropical static stability in response to decreasing CO₂,

which allows the subtropical eddies to shift poleward as consistent with previous studies (e.g., Lu et al. 2007, Son et al. 2018). Compared to the static stability, the baroclinicity change due to vertical wind shear is relatively weak. However, the vertical wind shear substantially contributes to a delay of the HC edge at the beginning of the RD period. Unlike the immediate response of Cst as the CO₂ change, Csh does not change much during the RU period and slightly increases after a few decades in the RD period. This suppressed vertical wind shear at the beginning of the RD period might partly cancel out the reduced static stability in the RD period.

The systematic changes of the baroclinicity due to static stability are also found in the NH as in the SH (Fig. 5b). It increases rapidly in the RU period, and slowly decreases in the RD period, with a switched sign at the middle of the RD period.

This sharp transition of Csh is coincident with a ToR of the northern HC edge (Fig. 5b), and importantly, it is manifest that this change in Csh results in the super recovery of the northern HC edge. Note that Csh change in the NH is greater than that in the SH, sufficiently affecting the super recovery of the northern HC edge. We thus conclude that wind shear plays a dominant role in creating a hemispheric asymmetry of the HC-edge changes, such as a delay in the SH but a super recovery in the NH, beyond the strong influences of static stability.

The above results reveal that the wind shear change primarily affects the less recovery of the HC edge in the SH but rather over-recovery in the NH. To further investigate these changes, it is important to note that previous studies claim the importance of the changed pattern of SST in shaping the HC edge by modulating the wind shear (Shaw and Voigt 2015, Zhou et al 2019). The change in the SST gradient, defined as the tropical SST (area-averaged over $0-20^{\circ}$) minus the midlatitude SST (area-averaged over $40^{\circ} -60^{\circ}$), is illustrated in Fig. 7 (black curves). By comparing Fig. 7 to Figs. 5, it is apparent that the patterns of SST gradient resemble that of wind shear changes. In the Southern Ocean, the SST gradient starts to decrease in the RD period and keeps the reduced gradient at the end of the RD (Fig. 7a). This reduction is mostly due to the Southern Ocean SST remaining warm after CO_2 removal (Fig. 6). Such a delayed response of the Southern Ocean has been well established in the literature (e.g., Manabe et al. 1990; Marshall et al. 2014). In the northern ocean, the Atlantic basin plays a pivotal role in overshooting the NH SST gradient (orange dashed lines in Fig. 7b). The Atlantic SST gradient remains unchanged during the RU period but sharply increases during the RD period, remaining positive at the end of the RD period (Fig. 6a). This pronounced SST change in the northern Atlantic Ocean results from the irreversible change of the Atlantic meridional overturning circulation (AMOC) after CO_2 removal (Ehlert

and Zickfeld 2018, An et al. 2021).

3.4. Hydro–climate implication of the HC change

Given the results in this study, our analyses are focused on the HC edge calculated by the PSI metric. In global climate models, the PSI metric is an accurate measure of the HC edge. However, we also examine the tropical edges with the P–E metric which is a good measure of the subtropical dry zone. The P–E metric–based HC edges show quantitatively similar results as in the PSI–based HC edge changes shown in Figs. 1b and 1c (Fig. 8). The changes in HC edge by P–E metric include the asymmetric characteristics of the PSI–based HC edges, i.e., a delay in the SH and a super recovery in the NH. Based on these similar results, an asymmetric hydrological change associated with the HC–edge is anticipated as in the literature (e.g., Chemke and Polvani 2019). Such HC–edge changes have immense hydrological implications on changes in weather and climate patterns, especially the occurrence of severe droughts around the world (Scheff and Frierson 2012, Feng and Fu 2013).

Calculation of the global dryness index (GDI; Lau and Kim 2015) suggests a possible hemispheric asymmetry of the aridity (Fig. 9). Overall, dryness is predominant over the land in both RU and RD periods as in the literature (Figs. 9a and 9b; see also Wu et al. 2010, Yeh et al. 2021). During the RU period, the global aridity becomes

enhanced over the subtropics, including California and Australia, except for the Arabian Peninsula. With a decreasing CO₂, these regions become wet, but in turn, the aridity is not fully removed. For instance, after CO₂ removal, the subtropics in the NH still remains drier than that in the PD state (Fig. 9c). Instead, the southern subtropics becomes wetter at the end of the RD period. This hemispheric–asymmetric aridity change implies that the asymmetric responses of the HC edge changes play a significant role in modulating the global aridity.

4. Summary and Discussions

We explore the responses of the HC edge in both hemispheres in the CO₂ removal scenario. Using the 28 ensemble members in the CESM1, changes of the HC edge over 140 years of decreasing CO₂ by 1% (RD) after 140 years of increasing CO₂ by 1% (RU) are examined. The hemispheric-asymmetric responses of the HC edges are pronounced to the CO₂ removal. In the SH, the HC edge shifts poleward greatly in the RU period but is delayed by a couple of decades at the beginning of the RD period. This delay results in the HC edge, remaining on the poleward side of its present-day (PD) state. Instead of the delay, the northern HC edge recovers over its PD state in the RD period. The northern edge rapidly shifts equatorward back in the RD period, even with a greater ratio than that in the RU period, remaining the HC edge located on the equatorward side of its PD state. Such distinct changes in both HC edges are largely explained by baroclinicity changes. Although most systematic changes are due to static stability change, the delay in the SH and a super recovery in the NH are more related to the unsystematically changed wind shear. In particular, the super recovery of the northern HC edge would be associated with the SST change over the Northern Atlantic Ocean. To be summarized, in response to CO₂ removal, the asymmetric responses of the HC edge

are a result of the hemispherically asymmetric changes of vertical wind shear changes associated with the SST.

To figure out the robustness of the above results, the results are compared to the eight models from the Coupled Model Intercomparison Project 6 (CMIP6; Eyring et al. 2016). The monotonic trends of the SH HC edge, which is found in the CESM-LE (Fig. 4a, 4b), are similarly shown in the CMIP6 models (Fig. 4c). The trends in the multi-model mean (MMM) of the CMIP6 models are $0.08 \pm 0.03^\circ \text{ decade}^{-1}$ in the RU and $-0.06 \pm 0.03^\circ \text{ decade}^{-1}$ in the RD period. It is apparent in Fig. 3a that the CESM-LE result is found within a range of the results from CMIP6 models. Compared to the SH, a larger intermodal spread is found in the NH among CMIP6 models (Fig. 4d). The CMIP6 MMM presents a large shifting trend in the RU ($0.01 \pm 0.02^\circ \text{ decade}^{-1}$) than that in the RD period ($-0.02 \pm 0.03^\circ \text{ decade}^{-1}$) in the NH. Most CMIP6 models provide increasing and decreasing trends in the RU and RD periods, respectively, except for CanESM5, CESM2, and NorESM2-LM. Importantly, the CESM-LEs have the highest RD trend than the CMIP6 models.

Notwithstanding the robust results from this study, the multi models in the CMIP6 archive exhibit a large uncertainty in the NH in response to the abrupt climate change (Fig. 4). However, it should be noted that only eight models are utilized here which provide a CDR

scenario. To reduce such uncertainties and fully understand the responses of the atmospheric circulation, especially in the NH, more models with large ensemble members should be considered.

References

- Allen, R. J., and Kovilakam, M., 2017: The role of natural climate variability in recent tropical expansion. *J. Clim.*, 30(16), 6329–6350.
- An, S. I., Shin, J., Yeh, S. W., Son, S. W., Kug, J. S., Min, S. K., and Kim, H. J., 2021: Global cooling hiatus driven by an AMOC overshoot in a carbon dioxide removal scenario. *Earth's Future*, 9(7), e2021EF002165.
- Boucher, O., and coauthors, 2012: Reversibility in an Earth System model in response to CO₂ concentration changes, *Environ. Res. Lett.*, 7(2), 024013.
- Cai, W., Cowan, T., and Thatcher, M., 2012: Rainfall reductions over Southern Hemisphere semi-arid regions: the role of subtropical dry zone expansion. *Scientific reports*, 2(1), 1-5.
- Chemke, R., and Polvani, L. M., 2019: Exploiting the abrupt 4 × CO₂ scenario to elucidate tropical expansion mechanisms. *J. Clim.*, 32(3), 859–875.
- Chou, C., J. D. Neelin, C.-A. Chen, and J.-Y. Tu, 2009: Evaluating the “Rich-Get-Richer” mechanism in tropical precipitation change under global warming, *J. Clim.*, 22(8), 1982–2005.
- Davis S. M., and Rosenlof K. H., 2012: A multidiagnostic intercomparison of tropical-width time series using reanalyses

- and satellite observations. *J. Clim.*, 25(4), 1061-1078.
- Davis, N. A., Seidel, D. J., Birner, T., Davis, S. M., and Tilmes, S., 2016: Changes in the width of the tropical belt due to simple radiative forcing changes in the GeoMIP simulations *Atmos. Chem. Phys.* 16(10) 083-10,095.
- D' Agostino R., P. Llonello, O. Adam, T. Schneider 2017: Factors controlling Hadley circulation changes from the Last Glacial Maximum to the end of the 21st century. *Geophys. Res. Lett.*, 44, 8585-8591.
- Eyring, V., S. Bony, G. A. Meehl, C. A. Senior, B. Stevens, R. J. Stouffer, and K. E. Taylor, 2016: Overview of the Coupled Model Intercomparison Project Phase 6 (CMIP6) experimental design and organization, *Geosc. Model Develop.*, 9(5), 1937–1958.
- Feng, S., and Q. Fu, 2013: Expansion of global drylands under a warming climate, *Atmospheric Chemistry and Physics*, 13, 10081–10094.
- Fu, R., 2015: Global warming–accelerated drying in the tropics. *Proceedings of the National Academy of Sciences*, 112(12), 3593-3594.
- Grise, K. M., and Davis, S. M., 2020: Hadley cell expansion in CMIP6 models. *Atmos. Chem. Phys.*, 20(9).
- Grise, K.M., S. M. Davis, I.R. Simpson, D. W. Waugh, Q. Fu, R. J. Allen, K. H. Rosenlof, C. C. Ummenhofer, K. B. Karlsruhkas, A. C.

- Maycock, and X. W. Quan, 2019: Recent tropical expansion: Natural variability or forced response?. *J. Clim.*, 32(5), 1551-1571.
- Hawkins, E., and Sutton, R., 2009: Decadal predictability of the Atlantic Ocean in a coupled GCM: Forecast skill and optimal perturbations using linear inverse modeling. *J. Clim.*, 22(14), 3960-3978.
- Hu, Y., and Q. Fu, 2007: Observed poleward expansion of the Hadley circulation since 1979. *Atmos. Chem. Phys.*, 7, 5229-5236, <https://doi.org/10.5194/acp-7-5229-2007>.
- Hu, Y., L. J. Tao, and J. P. Liu, 2013: Poleward expansion of the Hadley circulation in CMIP5 simulations. *Adv. Atmos. Sci.*, 30, 790-795, <https://doi.org/10.1007/s00376-012-2187-4>.
- Held, I. M., and B. J. Soden, 2006: Robust responses of the hydrological cycle to global warming, *J. Clim.*, 19, 5686-5699.
- Hurrell, J. W. et al., 2013: The community earth system model: a framework for collaborative research, *Bull. Am. Meteorol. Soc.*, 94, 1339-1360.
- Jackson, L.C., N. Schaller, R. S. Smith, M. D. Palmer, and M. Vellinga, 2014: Response of the Atlantic meridional overturning circulation to a reversal of greenhouse gas increases, *Clim. Dyn.*, 42(11), 3323-3336.
- Keller, D. P., A. Lenton, V. Scott, N. E. Vaughan, N. Bauer, D. Ji, ...

- and K. Zickfeld, 2018: The carbon dioxide removal model intercomparison project (CDRMIP): Rationale and experimental protocol for CMIP6, *Geosc. Model Develop.*, 11(3), 1133–1160.
- Kim, S. Y., and S. W. Son, 2020: Breakdown of the linear relationship between the Southern Hemisphere Hadley Cell Edge and Jet Latitude Changes in the Last Glacial Maximum. *J. Clim.*, 33(13), 5713-5725.
- Lau, W. K. M., and K.-M. Kim, 2015: Robust Hadley Circulation changes and increasing global dryness due to CO₂ warming from the CMIP5 model projections, *Proc. Natl. Acad. Sci. USA*, 112, 3630–3635.
- Lu, J., G. A. Vecchi, and T. Reichler, 2007: Expansion of the Hadley cell under global warming, *Geophys. Res. Lett.*, 34, L06805.
- Lu, J., Chen, G., and Frierson, D. M., 2008: Response of the zonal mean atmospheric circulation to El Niño versus global warming. *J. Clim.*, 21(22), 5835-5851.
- Manabe, S., Bryan, K. and, Spelman, M. J., 1990: Transient response of a global ocean-atmosphere model to a doubling of atmospheric carbon dioxide. *J. Phys. Oceanogr.* 20, 722-749.
- Mantsis, D. F., Sherwood, S., Allen, R., and Shi, L., 2017: Natural variations of tropical width and recent trends. *Geophys. Res. Lett.*, 44(8), 3825-3832.
- Marshall, J. et al., 2014: The ocean’ s role in polar climate change:

- asymmetric Arctic and Antarctic responses to greenhouse gas and ozone forcing. *Phil. Trans. R. Soc. A* 372, 20130040.
- Scheff, J., and D. M. W. Frierson, 2012: Robust future precipitation declines in CMIP5 largely reflect the poleward expansion of model subtropical dry zones, *Geophys. Res. Lett.*, 39, L18704.
- Seager, R. 2007: Model projection of an imminent transition to a more arid climate in southwestern North America, *Science*, 316, 1181–1184.
- Seidel, D. J., Q. Fu, W. J. Randel, and T. J. Reichler, 2008: Widening of the tropical belt in a changing climate. *Nat. Geosci.*, 1, 21–24, <https://doi.org/10.1038/ngeo.2007.38>.
- Solomon, A., L. M. Polvani, D. W. Waugh, and S. M. Davis, 2016: Contrasting upper and lower atmospheric metrics of tropical expansion in the Southern Hemisphere. *Geophys. Res. Lett.*, 43, 10 496–10 503, <https://doi.org/10.1002/2016GL070917>.
- Son, S.–W., B. R. Han, C. I. Garfinkel, S. Y. Kim, R. Park, N. Abraham, G. Zeng, and coauthors, 2018a: Tropospheric jet response to Antarctic ozone depletion: an update with Chemistry–Climate Model Initiative (CCMI) models. *Environ. Res. Lett.*, 13, 054024.
- Son, S.–W., S. Y. Kim, and S. K. Min, 2018b: Widening of the Hadley cell from Last Glacial Maximum to future climate. *J. Climate*, 31(1), 267–281.
- Staten, P., W., and T. Reichler, 2014: On the ratio between shifts in

- the eddy-driven jet and the Hadley cell edge. *Clim. Dyn.*, 42, 1229-1242, doi:10.1007/s00382-013-1905-7.
- Tandon, N. F., Gerber E. P., Sobel, A. H., Polvani, L. M., 2013: Understanding Hadley Cell Expansion versus Contraction: Insights from Simplified Model and Implication for Recent Observations. *J. Clim.*, 26, 4304-4321.
- UNFCCC, 2016: Paris Agreement of the 21st session of the Conference of Parties on climate change.
- Walker, C. C., and T. Schneider, 2006: Eddy influences on Hadley circulations: Simulations with an idealized GCM. *J. Atmos. Sci.*, 63, 3333-3350, <https://doi.org/10.1175/JAS3821.1>.
- Watt-Meyer, O., D. M. W. Frierson, and Q. Fu., 2019: Hemispheric asymmetry of tropical expansion under CO₂ forcing. *Geophys. Res. Lett.*, 46, 9231-9240.
- Waugh, D. W., K. M. Grise, W. J. M. Seviour, S. M. Davis, N. Davis, O. Adam, and coauthors, 2018: Revisiting the relationship among metrics of tropical expansion. *J. Climate*, 31(18), 7565-7581.
- Wigley T M L 2005 The climate change commitment *Science* 307 1766-9
- Wu, P., J. Ridley, A. Pardaens, R. Levine, and J. Lowe, 2015: The reversibility of CO₂ induced climate change, *Clim. Dyn.*, 45(3), 745-754.

Figures

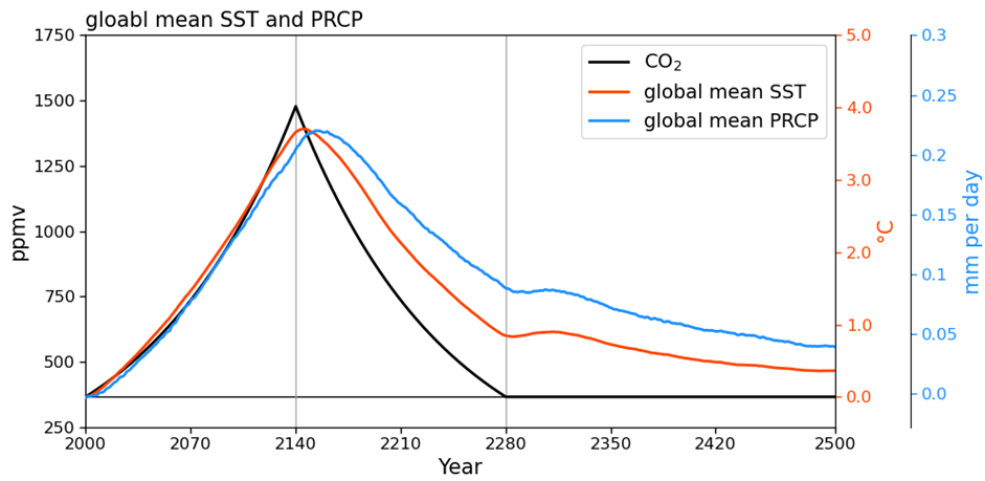


Fig. 1. Time series of CO₂ concentration (black), global mean sea surface temperature (SST, red), and global mean precipitation (PRCP, blue), respectively. Red and blue solid lines indicate the 28-member ensemble mean, and a black horizontal line indicates the PD state of CO₂ concentration.

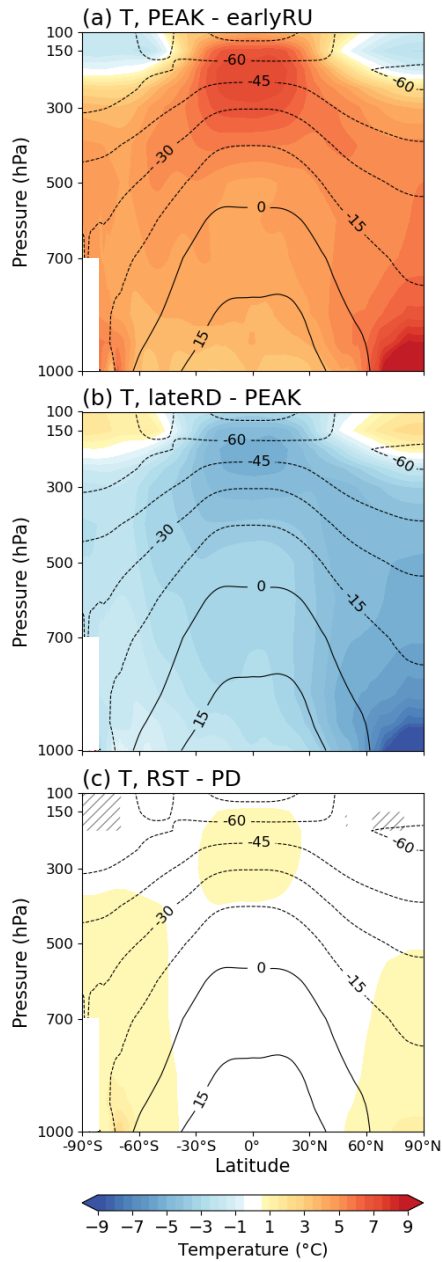


Fig. 2. Spatial distribution for the 28-ensemble mean of the zonal-mean temperature (units: °C) changes. (a) is the changes during the RU period computed by PEAK (2120–2160) minus earlyRU (2001–2040), and (b) is during the RD period computed by the lateRD (2241–2280) minus PEAK (2120–2160). (c) is the difference between RST period (2281–2320) and PD state. Contours indicate the climatology in the PD experiment and hatching denotes regions where the difference is statistically insignificant based on Student's t-test estimates at the 95% level.

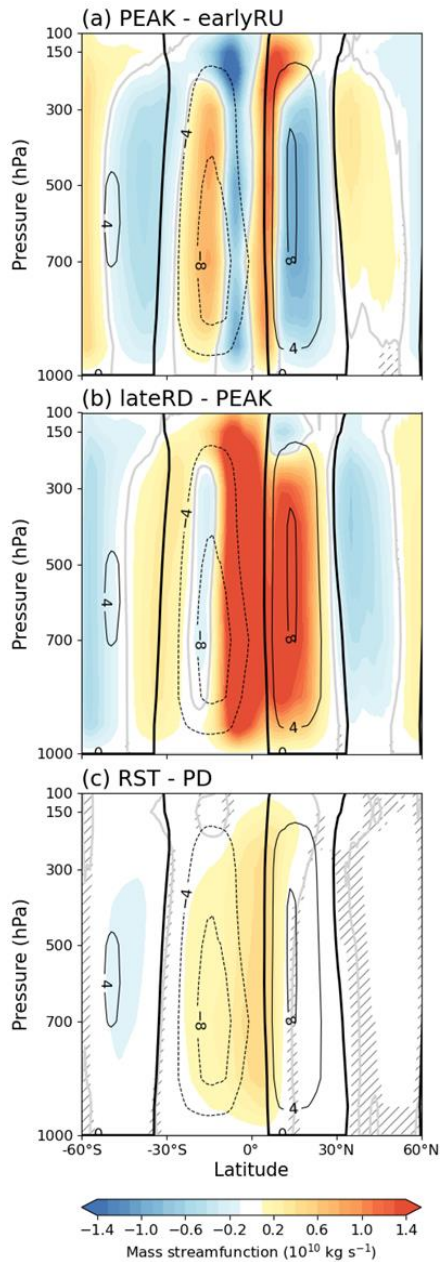


Fig. 3. Spatial distribution for the 28-ensemble mean of meridional streamfunction (units: $10^{10} \text{ kg s}^{-1}$) changes. (a) is the changes during the RU period computed by PEAK (2120–2160) minus earlyRU (2001–2040), and (b) is during the RD period computed by the lateRD (2241–2280) minus PEAK (2120–2160). (c) is the difference between RST period (2281–2320) and PD state. Contours indicate the climatology in the PD experiment and hatching denotes regions where the difference is statistically insignificant based on Student’ s t-test estimates at the 95% level.

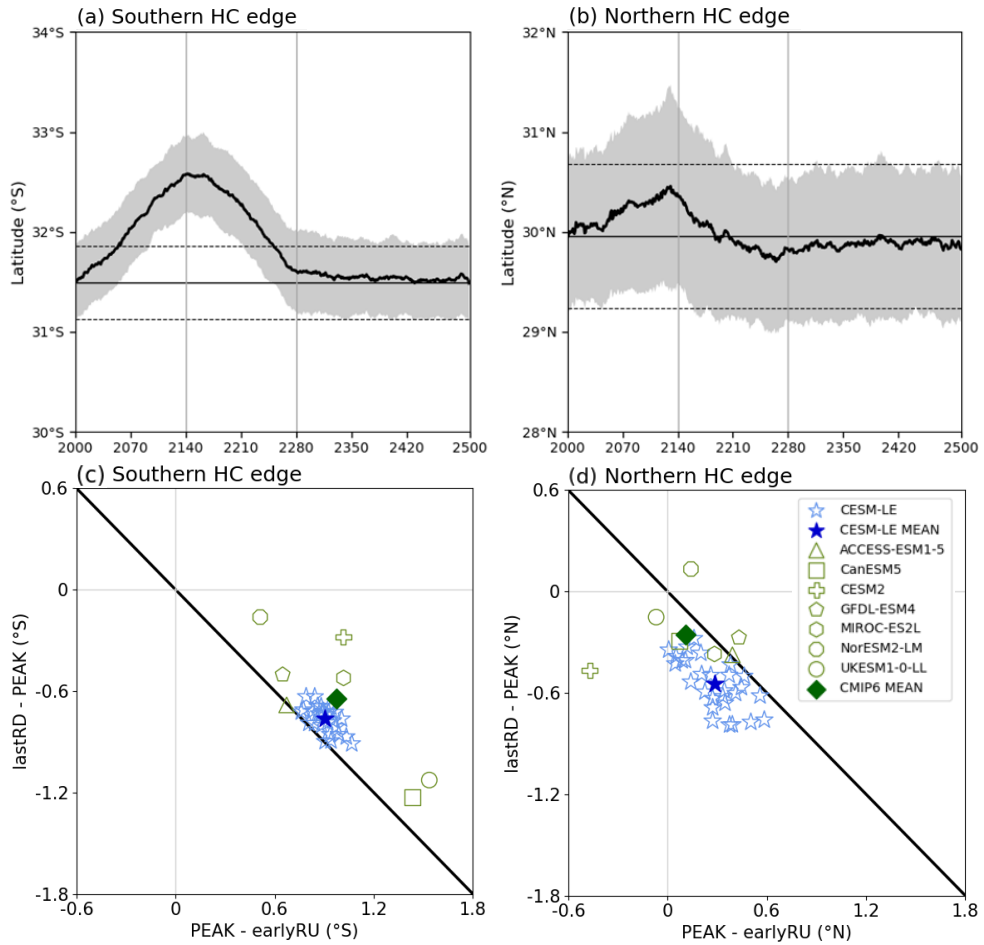


Fig. 4. The HC edge changes in (a), (c) the southern hemisphere, and (b), (d) the northern hemisphere. (a), (b) the time evolutions of the HC edge for a changing CO₂ pathway. The thick solid lines and shadings denote the mean and one-standard deviation range of 28 ensembles smoothed with an 11-yr running mean, respectively. The mean and one-standard deviation range in the PD run are denoted by horizontal solid and dashed lines, respectively. (c), (d) the relationship between changes of the HC edge during the RU and RD period. Changes during the RU and RD period are computed by PEAK (2120–2160) minus earlyRU (2001–2040), and by lateRD (2241–2280) minus PEAK. Blue and green symbols indicate the results of CESM-LE and CMIP6, respectively.

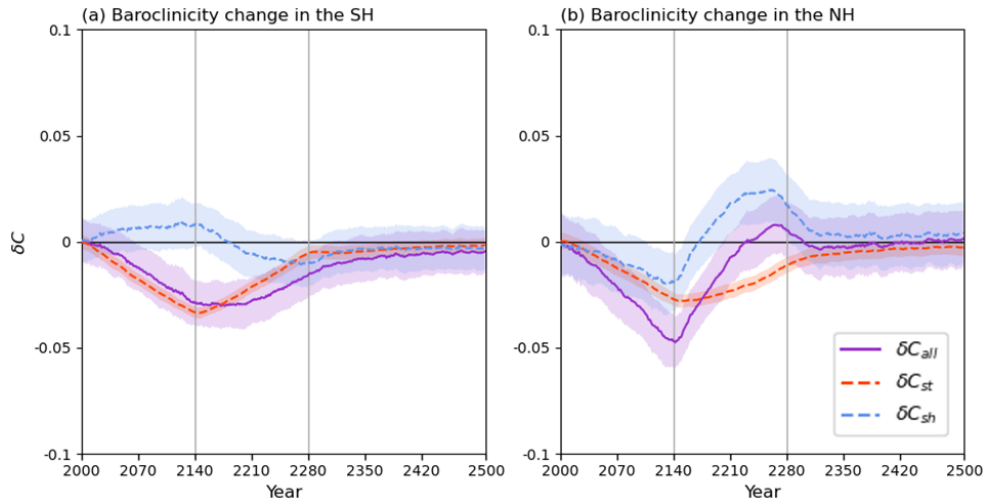


Fig. 5. Time evolution of baroclinicity anomalies over the (a) southern and (b) northern hemispheres relative to the PD run. The solid and dashed lines denote the mean of 28 ensembles, and shadings indicate the one-standard deviation range of that. Purple, red, and blue correspond to the baroclinicity changes due to both static stability and wind shear, only due to static stability, and only due to wind shear, respectively.

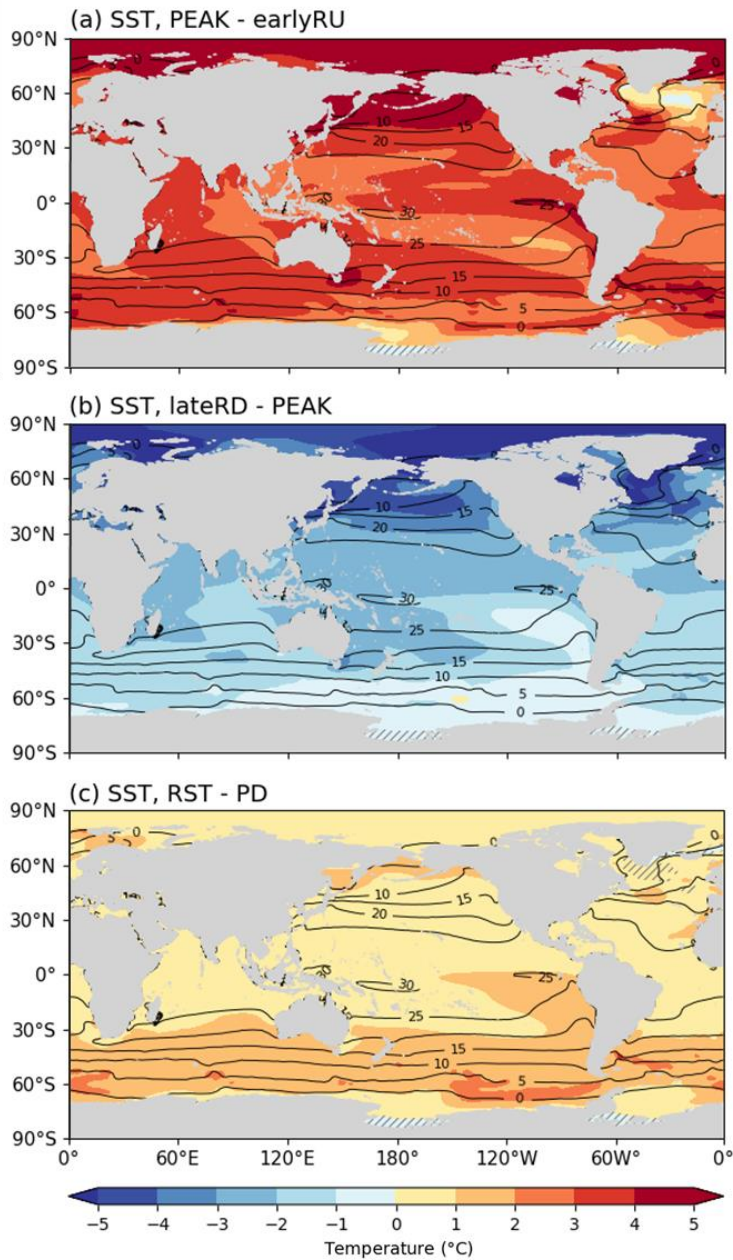


Fig. 6. Spatial distribution for the 28-ensemble mean of sea surface temperature (SST, units: ° C) changes. (a) is the changes during the RU period computed by PEAK (2120–2160) minus earlyRU (2001–2040), and (b) is during the RD period computed by lateRD (2241–2280) minus PEAK (2120–2160). (c) is the difference between RST period (2281–2320) and PD state. Contours indicate the climatology in the PD experiment and hatching denotes regions where the difference is statistically insignificant based on Student’s *t*-test estimates at the 95% level.

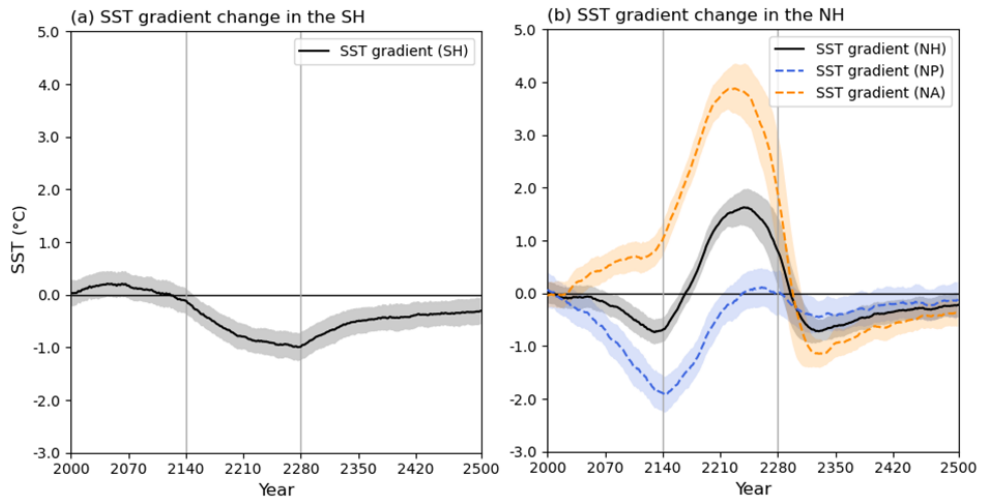


Fig. 7. (a) Time evolution of SST gradient anomalies (units: °C) relative to the PD run over the Southern hemisphere (SH; black). (b) Same as (a) but for the Northern hemisphere (NH; black), the North Pacific (NP; 120° E – 90° W, pink dashed), and the North Atlantic (NA; 70° W–20° E, red dashed). The SST gradient implies the latitudinal gradient calculated by the SST differences from the tropics (0° –15° latitude) to the mid-latitudes (45° –60° latitude) in each hemisphere. The solid and dashed lines denote the 28-member ensemble mean smoothed with an 11-yr running mean, and shadings indicate the one-standard deviation range of that.

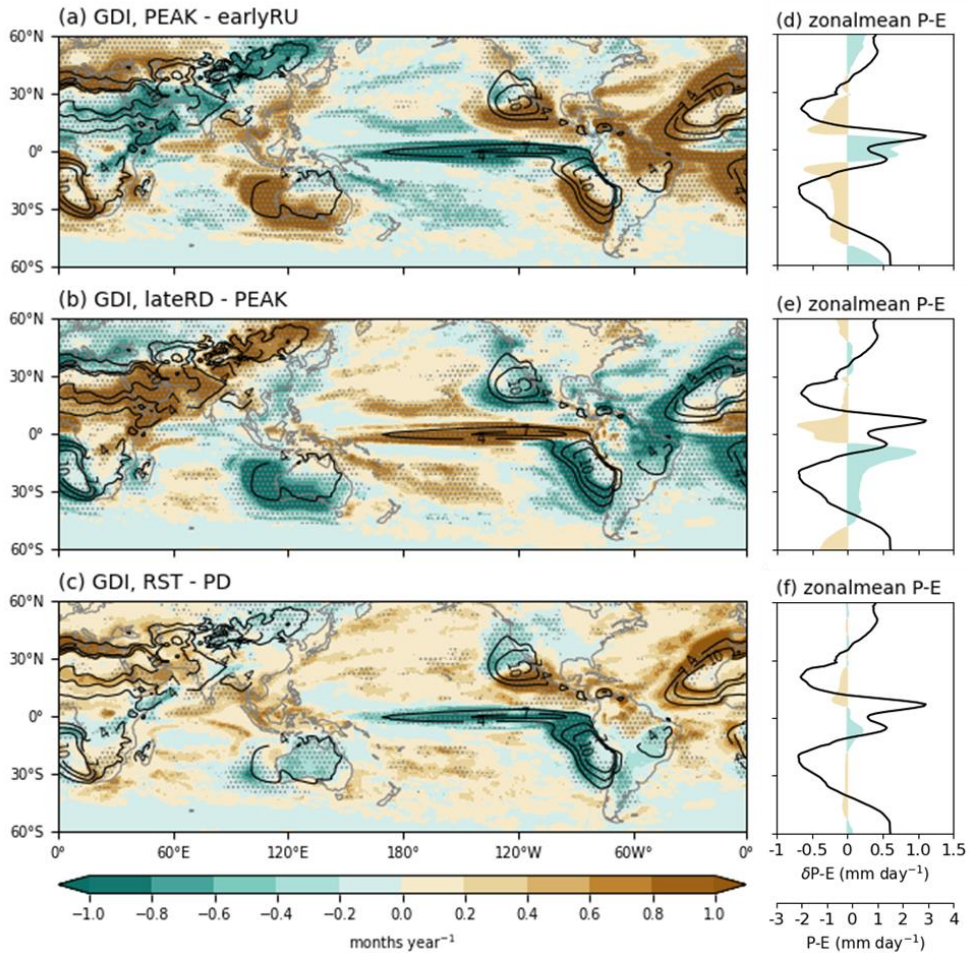


Fig. 8. Spatial distribution for the 28-ensemble mean of the GDI (left, unit: months year⁻¹) and zonal-mean P-E changes (right, units: mm day⁻¹). (a), (d) is the changes during RU period computed by PEAK (2120–2160) minus earlyRU (2001–2040), and (b), (e) is during the RD period computed by the lateRD (2241–2280) minus PEAK (2120–2160). (c), (f) is the difference between RST (2280 - 2320) and PD state. Contours in (a)–(c) are the climatological GDI in the PD experiment. Dotted regions denote the statistically insignificant difference based on Student’s t-test estimates at the 95% level. The colored area in (d)–(f) indicates negative (brown) and positive (green) P-E differences ($\delta P-E$), and black lines denote the climatological zonal-mean P-E in the PD experiment.

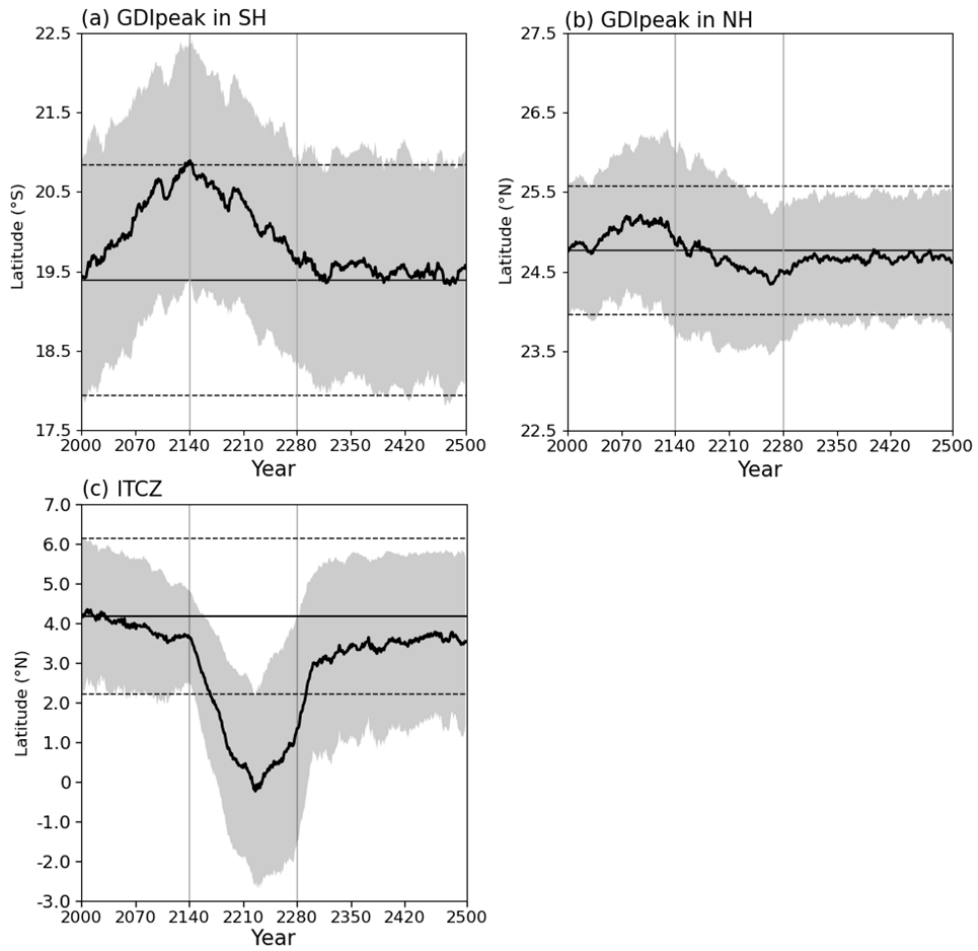


Fig. 9. Time evolution of the GDI peak in (a) southern and (b) northern hemispheres, and (c) ITCZ for a changing CO₂ pathway. The thick solid lines and shadings denote the mean and one-standard deviation range of 28 ensembles smoothed with an 11-yr running mean, respectively. The mean and one-standard deviation range in the PD run are denoted by horizontal solid and dashed lines, respectively.

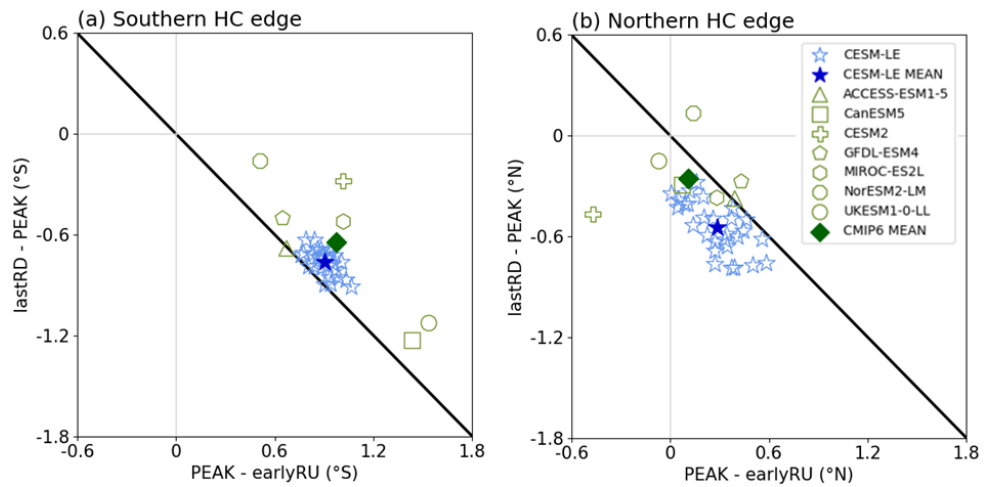


Fig. 10. Relationship between changes of the HC edge during the RU and RD periods in the (a) southern and (b) northern hemispheres. Changes during the RU period computed by PEAK (2120–2160) minus earlyRU (2001–2040), and (b) is during the RD period computed by the last RD (2241–2280) minus PEAK (2120–2160).

국문 초록

이산화탄소 증가 및 감소에 따른 해들리셀 경계의 비대칭적인 반응

최영주

협동과정 계산과학

서울대학교 대학원

전지구 수문 수지를 결정하는 중요한 역할을 하는 해들리셀 경계는 지구온난화에 따라 극방향으로 확장하는 것으로 알려져 있다. 기후 모형을 이용한 선행연구에서는 이산화탄소 증가에 따른 해들리셀 연구에 집중되어 왔다. 본 연구에서는 이산화탄소 증가 및 감소에 따른 남북반구 해들리셀 경계의 변화를 살펴보았다. 이를 위해 CESM1.2 모형을 이용하여 이산화탄소 농도를 2000년대 수준(367 ppm)에서 매년 1%씩 증가시킨 후 같은 비율로 감소시킨 시나리오를 분석하였다. 이산화탄소 농도 증가에 따라 남북반구 해들리셀 경계는 모두 극방향으로 이동하는 양상을 보였으나, 이산화탄소 농도 감소에 대해 남반구 해들리셀 경계는 느리게 반응하고 북반구 해들리셀 경계는 빠르게 반응하는 특징을 보였다. 그 결과 이산화탄소 농도가 원래 수준으로 돌아왔을 때 해들리셀의 경계는 남반구는 원래 위치로 돌아오지 못해 극방향에 머무른 반면, 북반구는 원래 위치를 지나 적도 방향에 위치하였다. 남북반구 해들리셀 경계의 비대칭적인 반응은 이산화탄소 감소 시기에 나타난 북반구 중위도 대류권 연직 바람시어의 급격한 변화에서 비롯된 것으로 확인되었다. 이는 이산화탄소 증감에

따른 해수면 온도의 반응 속도의 차이와 관련 있는 것으로 나타났다. 비롯된 북반구 중위도 대류권 연직 바람 시어의 급격한 변화에서 연관된 것으로 확인되었다. 이러한 남북반구 해들리셀 경계의 변화는 아열대 지역의 건조 기후의 가역성에도 영향을 미칠 수 있음을 시사한다.

주요어 : 해들리셀, 이산화탄소 농도, 해수면 온도, baroclinicity

학 번 : 2020-24660